# A CFD−DEM study on the suffusion and shear behaviors of gap-graded soils under stress anisotropy

**Authors:**

Z. Hu[a,b], J. Z. Li[a], Y. D. Zhang[c,*], Z. X. Yang[b], J. K. Liu[a]

**Affiliations:**

[a] School of Civil Engineering, Sun Yat-sen University & Southern Marine Science and Engineering Guangdong Laboratory, Zhuhai, Guangdong, 519082, China

[b] MOE Key Laboratory of Soft Soils and Environmental Engineering, Computing Center for Geotechnical Engineering (COMEGE), Department of Civil Engineering, Zhejiang University, Hangzhou, Zhejiang, 310058, China

[c] Department of Civil, Environmental and Architectural Engineering, University of Colorado Boulder, Boulder, Colorado, 80309, USA

**Corresponding Author:**

[*] E-mail address: Yida.Zhang@Colorado.EDU (Y. D. Zhang).

## Abstract

This study investigates the evolution of suffusion and mechanical behaviors of gap-graded soils under anisotropic stress conditions. The interactions between granular assembly and seepage flow are modeled using the coupled computational fluid dynamic and discrete element method (CFD−DEM). A series of suffusion tests followed by drained triaxial compression and extension tests are performed to explore the influence of stress anisotropy on the initiation and development of suffusion and the shear responses of eroded specimens. The results reveal that the specimens with the major principal effective stress aligned with the primary flow direction are more erodible evidenced by more severe fines loss, volumetric contraction, and void ratio changes. Suffusion tends to reduce the peak strength, peak friction angles, and secant stiffness of specimens under both triaxial compression and extension conditions, while its impact on the critical-state shear strength is negligible. The change of contact network efficiency is tracked by various coordination number measures during the suffusion and shear stages. The evolution of stress anisotropy during suffusion and shearing is evaluated by the directional distributions of the strong and weak normal contact forces.



**Keywords**: suffusion; fabric anisotropy; CFD−DEM; microstructure; shear behaviors

# 1. Introduction

Internal erosion is one of the culprits for the instability and even dysfunction of earthworks, such as foundations, dams and levees [1–3]. Since the last century, approximately half of all dam failures have been caused by internal erosion in different forms, including concentrated leak erosion, backward erosion, soil contact erosion and suffusion [4]. This study focuses on suffusion, which refers to the process of fine particles being detached and transported through the soil matrix by seepage flow. It has been well recognized that the onset and evolution of suffusion are closely related to many factors, e.g., geometric conditions [5–8], stress states and history [9–11], and hydraulic conditions [12, 13]. Among the extensive suffusion investigations in recent years [14–16], the influences of stress conditions on suffusion have attracted much attention due to its complexity and ubiquity in earthen structures. Specifically, in embankment dams, both stress and hydraulic conditions vary with locations. The soils inside dams are usually in anisotropic stress states with the maximum principal effective stress being oblique and having an angle varying from 0 ~ 90° with respect to the primary flow direction [17].

Although the full suffusion process and its effect on mechanical behaviors of soils can be conveniently studied through laboratory tests [4, 18–20] and modeled through continuum-based numerical simulations, e.g., finite element method [21, 22], the underlying mechanism of suffusion is still unclear due to the lack of microscopic observations and quantifications. To examine the microscopic processes during suffusion, the discrete element method (DEM) is commonly adopted for its advantages in detecting the structural characteristics of soils under various stress conditions at any time step [23]. Muir Wood et al. [24] is possibly the first to investigate mechanical behaviors of erodible soils by removing fine particles randomly in two-dimensional (2D) DEM simulations, and found that the gradation has a first-order influence on critical states of soils. Luc Scholtès et al. [25] and Zhang et al. [26] investigated the triaxial shear behaviors of eroded soils by deleting a designated percent of inactive fine particles which carry relatively low contact forces, and found that the shear behaviors

and flow field of soils are greatly modified by particle removal. On the other hand, the migrations of fine particles during suffusion are normally accompanied by the repetitive clogging-unclogging phenomenon, i.e., some fine particles could be restrained inside the voids among soil skeleton and regain freedom by seepage forces. This could result in a transient evolution of microstructure and thus the mechanical behavior of soils, which cannot be captured by the DEM simulations using conventional particle removal schemes [27, 28]. More recently, the combination of computational fluid dynamics and discrete element method (CFD−DEM) has also been developed and demonstrated to be of high efficiency and accuracy in simulating the intricate solid−fluid interactions using multiple CFD solvers [29–32]. In the most commonly adopted unsolved CFD−DEM scheme, the fluid cells are coarsely discretized to be several times greater than the particle sizes, and the flow field is volume-averaged within a local space by solving the locally averaged Navier-Stokes equation. On this basis, it has several fundamental limitations. First, only single-phase flow through spherical particles can be considered [11, 33]. Second, the particle-fluid interactions are normally estimated using empirical methods and require extensive validations [34, 35]. Additionally, the fluid mesh is fixed and cannot be applied to moving boundary problems [36, 37]. However, in the very recent years, these limitations have been partially eliminated by incorporating irregular particle shapes, moving flow filed, and multi-phase flow [38–41]. In the authors' previous works, an open-source CFD−DEM package was used to simulate the full suffusion process under the designated confining pressure, tracking the rearrangement of particles and the variations in contact networks of gap-graded soils with different fines content [42]. Further investigations on the mechanical responses of eroded soils under drained and undrained triaxial compression conditions revealed that suffusion causes distinct reduction of peak shear strength of soils, which is comparable to the experimental results on eroded soils [43–46]. However, in these studies, soil specimens were mainly deposited under gravity or consolidated under isotropic confining pressure. This oversimplifies the in-situ stress conditions often encountered in earthworks where stress anisotropy and non-coaxiality between flow and principal stress direction prevail.

It is well known that the stress anisotropy has a significant effect on the structure of soil matrix, and thus the mechanical behaviors of soils [47–49]. Oda et al. [50] investigated the impact of the initial anisotropic stress states on the microstructure of soils, and found that new contacts were generated along the major principal effective stress direction. Yang et al. [51] investigated the anisotropy effect on undrained behaviors of soils using DEM, and found that the mechanical behaviors and dilatancy vary dramatically for specimens with different fabric anisotropy intensity, while the critical-state shear strength is rather independent of the initial fabric. Gu et al. [52] simulated the drained triaxial shear and simple shear tests on specimens with different stress states, and found that the initial fabric and contact force anisotropy results in significant anisotropy in stiffness. Since stress anisotropy alters the force chain network which also critically impacts the stress states of fine particles, it is intuitive to assume a strong interplay between stress anisotropy and the erodibility of fines as well. On this basis, Chang et al. [17] modified a triaxial apparatus for suffusion modeling, and found the larger initial stress ratio contributes to the greater erosion rate of specimens for a given hydraulic gradient. Through similar experiments, Luo et al. [53] investigated the influence of deviatoric stress on critical hydraulic gradients of suffusion, and proposed an empirical method for estimating the critical hydraulic gradient under complex stress conditions. From the simulation aspects, Ma et al. [16] studied the effect of flow direction on the microscopic mechanism of particle detachment and migration during suffusion, and found that the anisotropic stress state is responsible for directional variations of microstructure of soils during suffusion. Qian et al. [54] and Xiong et al. [55] presented the evolution of stress anisotropy caused by suffusion considering the effect of irregular particle shapes, and concluded that the angularity intensifies suffusion resistance and shear strength of soils.

In this study, the influence of stress anisotropy is investigated on suffusion and shear behaviors of gap-graded soils using CFD−DEM. This study differs from our previous works [13, 28, 42] by focusing on anisotropically stressed specimens, aiming to quantify the effect of stress anisotropy on their suffusion and shearing responses. The

methodology and simulation procedure of suffusion and triaxial shearing are presented in Section 2. The evolution of the fines loss and volumetric deformation are reproduced for the full suffusion process. The shear responses of both non-eroded and eroded specimens under different stress paths are discussed in Section 3. The microstructural changes, including the coordination numbers, the contact force chain networks, and the stress anisotropy quantified by the fabric tensor are elaborated and used to interpret the observed suffusion and shear responses in Section 4.

## 2. Simulation procedure

The adopted CFD−DEM approach is an amalgam of the DEM package LIGGGHTS and the CFD package OpenFOAM [56]. Details of this methodology and its validation/benchmarking can be found in Tsuji et al. [33] and our previous works [13, 28, 42], so will be not repeated here for brevity.

The simulation process consists of four consecutive steps: particle insertion, consolidation, suffusion and triaxial shearing, as illustrated in Fig. 1. First, in the particle insertion stage, a cubic specimen with 40,000 particles is first generated and enclosed by six rigid frictionless walls with a dimension of 25 mm × 25 mm× 25 mm. The sizes of fine and coarse particles range between 0.42 ~ 0.5 mm and 2.08 ~ 2.4 mm, respectively. The fines content ($FC$) of the non-eroded specimen is $FC$ = 35% by mass, which is internally unstable according to the criteria of Kenney and Lau [57]. The grain size distributions (GSDs) of all non-eroded and eroded specimens subjected to different stress conditions are shown in Fig.2. Since the adopted CFD−DEM method is a locally averaged coarse-grid method, the recommended size of the fluid cell is taken 2 ~ 4 times that of the average particle size, which has been demonstrated to yield the appropriate and sensible results [58–60]. The input parameters used in the simulations are listed in Table 1, which are the same as our previous work [13, 28]. Similar parameters were also used in many other CFD−DEM studies, e.g., Shan and Zhao [61], Li and Zhao [62], Mu et al. [37]. The simulations were performed using a workstation with 168G RAM and 2 × 20-core 2.5 GHz CPU. The solid and fluid regions were

equally decomposed into 8 subdomains using 8 cores (2 × 2 × 2 in $x$, $y$ and $z$ directions). The simulation of suffusion process for $t$ = 15s takes about 72 hours computation time.

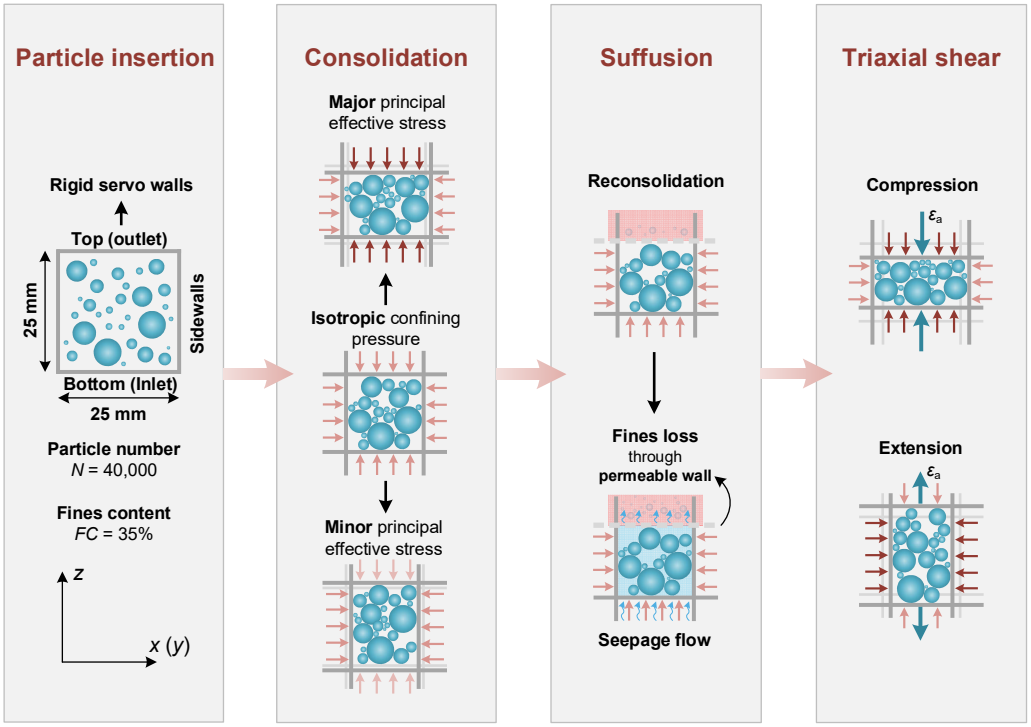


**Fig. 1** Procedure of particle insertion, consolidation, suffusion and triaxial shear

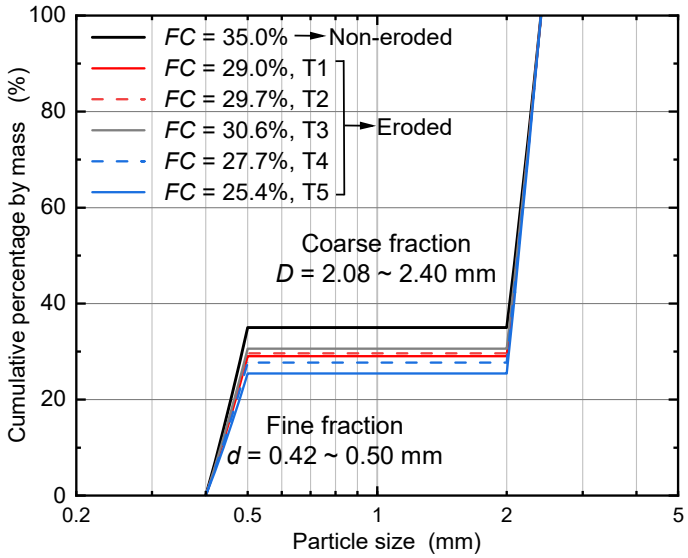


**Fig. 2** Grain size distributions (GSDs) of tested specimens

**Table 1** Input parameters used in the simulations

| Computation modules | Parameter types | values |
|---|---|---|
| Solid phase (DEM) | Particle number | 40,000 |
| | Fine particle diameter (mm) | 0.42 ~ 0.5 |
| | Coarse particle diameter (mm) | 2.08 ~ 2.4 |
| | Particle density (kg/m$^3$) | 2,650 |
| | Young's modulus (GPa) | 70 |
| | Poisson's ratio | 0.3 |
| | Coefficient of friction | 0.5 |
| | Coefficient of restitution | 0.2 |
| | Coefficient of rolling friction | 0.1 |
| | Acceleration of gravity (m/s$^2$) | 9.8 |
| Fluid phase (CFD) | Fluid density (kg/m$^3$) | 1,000 |
| | Dynamic viscosity (Pa·s) | $1\times10^{-3}$ |
| | Size of fluid cells (mm) | 3.2 |
| Solid−fluid interaction (CFD-DEM) | Timestep of DEM (s) | $2\times10^{-7}$ |
| | Timestep of CFD (s) | $2\times10^{-5}$ |
| | Coupling interval (s) | $2\times10^{-5}$ |
| | Simulation duration (s) | 15 |

In the consolidation stage, all specimens are first isotropically confined to the same effective stress, i.e., $p'$ = 100 kPa. The interparticle coefficient of friction is set to $\mu_{f0}$ = 0.1 to generate a relatively dense specimen. After reaching equilibrium, the interparticle coefficient of friction is restored to $\mu_f$ = 0.5, as commonly adopted in other DEM studies [63]. The rolling resistance is also employed with the coefficient of restitution $\mu_r$ = 0.1 to approximately account for the effect of irregular particle shapes [42]. For the preparations of the initially stress anisotropic specimen, the axial stress is progressively increased or decreased to the designated stress ratios $\eta = q / p'$, depending on triaxial compression or extension shearing, where $p' = (\sigma'_a + 2\sigma'_r) / 3$ is the mean effective stress, $q = \sigma'_a - \sigma'_r$ is the deviatoric stress, and $\sigma'_a$ and $\sigma'_r$ are the axial and radial effective stresses, respectively. Five specimens with different initial stress ratios $\eta$ are generated as illustrated in Fig. 3, and their stress conditions and initial void ratios are summarized in Table 2. It is seen from Table 2 that, all specimens have almost the same initial void

ratio around $e_0$ = 0.40 even under different stress states. After completing the above steps, gravity is activated and maintained until the end of the erosion process. The reason for not activating gravity in consolidation is to prevent the potential segregation and accumulation of fine particles at the bottom of specimens during sample preparation.

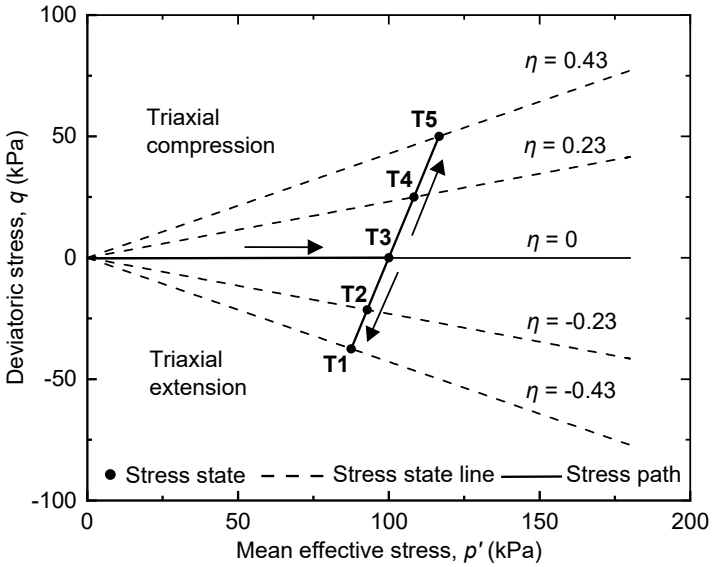


**Fig. 3** Initial stress states of the non-eroded specimens

**Table 2** Stress conditions of the simulation cases

| Specimen IDs | Radial effective stress, $\sigma'_r$ (kPa) | Axial effective stress, $\sigma'_a$ (kPa) | Mean effective stress, $p'$ (kPa) | Deviatoric stress, $q$ (kPa) | Initial stress ratio, $\eta_0$ | Initial void ratio, $e_0$ |
|---|---|---|---|---|---|---|
| T1 | 100 | 62.5 | 87.5 | -37.5 | -0.43 | 0.400 |
| T2 | 100 | 78.6 | 92.9 | -21.4 | -0.23 | 0.399 |
| T3 | 100 | 100 | 100 | 0 | 0 | 0.398 |
| T4 | 100 | 125 | 108.3 | 25 | 0.23 | 0.399 |
| T5 | 100 | 150 | 116.7 | 50 | 0.43 | 0.397 |

In the suffusion stage, the top boundary wall is changed to a permeable wall that allows for the free penetration of fine particles while restraining coarse particles inside the specimen. This could result in a slight relaxation of confining pressure, and thus a reconsolidation procedure is followed to regain the target stress state of the specimen [34, 42]. Thereafter, an upward seepage flow is introduced by imposing the pore

pressure difference between top and bottom boundaries of the fluid domain. The four horizontal boundaries are set as undrained boundaries to maintain one-dimensional flow. The detailed boundary conditions for the CFD and DEM domains during suffusion are listed in Table 3. The stress state is maintained constant during the full suffusion process. To mitigate the excessive skeleton disturbance caused by the sudden change of hydraulic conditions, the hydraulic gradient starts at zero and is gradually increased via several stages as illustrated in Fig. 4. Note that the suffusion in real earthworks is a long-term process and could hardly be reproduced by the adopted simulation scheme. Therefore, the maximum hydraulic gradient is set large (i.e., $i_{max}$ = 10) so that the majority of fines loss can be reproduced in a short seepage period [28] (i.e., $t$ = 15s).

**Table 3** Boundary conditions during suffusion

| | CFD boundaries | DEM boundaries |
|---|---|---|
| Bottom (Inlet) | Pore pressure: $u_{in} = u_0$<br>Velocity gradient: $\partial \boldsymbol{U}_f / \partial z = 0$ | Effective stress: $\sigma'_{zz} = p'$<br>Impermeable to fines |
| Top (Outlet) | Pore pressure: $u_{out} = 0$<br>Velocity gradient: $\partial \boldsymbol{U}_f / \partial z = 0$ | Fixed: $\delta_{zz} = 0$<br>Permeable to fines |
| Sidewalls | Pore pressure gradient:<br>$\partial u / \partial x = 0$, or $\partial u / \partial y = 0$<br>Velocity: $\boldsymbol{U}_f \cdot \boldsymbol{n} = 0$ where $\boldsymbol{n}$ is the unit normal vector of the sidewalls | Effective stress: $\sigma'_{xx} = \sigma'_{yy} = p'$<br>Impermeable to fines |

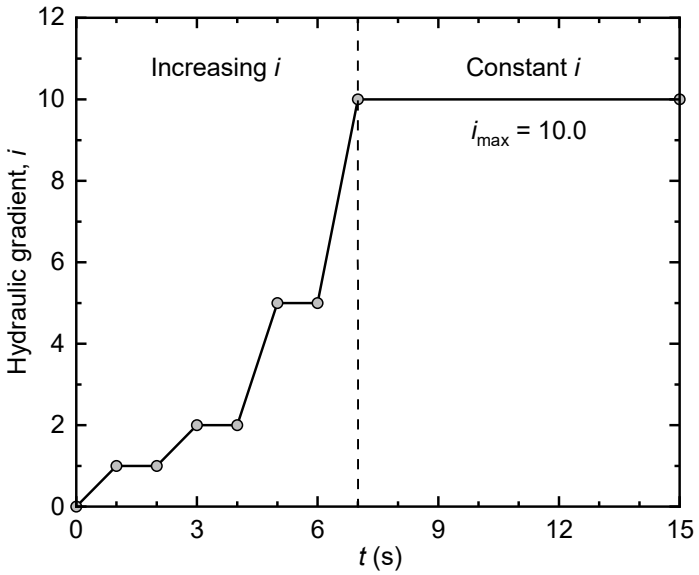


**Fig. 4** Variation of the hydraulic gradient with elapsed time

Once suffusion is completed, the permeable top boundary wall is changed to an impermeable wall, and a series of drained triaxial shear tests are performed on all specimens at a small strain rate (i.e., $\dot{\varepsilon} = 0.025$ s$^{-1}$) at which the quasi-static condition is satisfied [28, 64]. The triaxial compression tests are performed on specimens with the positive stress ratio $\eta$, i.e., the major principal effective stress on the longitudinal direction, and the others are subjected to triaxial extension tests. The radial effective stress is maintained constant during the entire shearing process, i.e., $\sigma'_r = 100$ kPa. For comparison, both the triaxial compression and extension tests are conducted on the non-eroded specimen. Note that gravity is not considered during shearing to be consistent with the conventional DEM simulations [28, 65].

# 3 Simulation results

## 3.1 Visualization of stress anisotropy of specimens

The particle assemblies and force chain networks of three typical specimens with multiple stress anisotropy, i.e., T1, T3, and T5 specimens, are presented in Fig. 5. It is found that all specimens lose some fine particles at the permeable top boundary, resulting in the local concentration of distinct (thick) primary force chains before suffusion [28]. Comparison of the force chain networks between different specimens clearly shows the effect of stress anisotropy: several distinct (thick) primary force

chains are formed towards the horizontal direction for the T1 specimen with the horizontal major principal effective stress. Conversely, the primary contact force chains of the T5 specimen are mainly distributed in the longitudinal direction, coincident with the vertical major principal stress direction. The contact force chains of the isotropic T3 specimen are distributed evenly inside the specimen except for those near the top boundary.

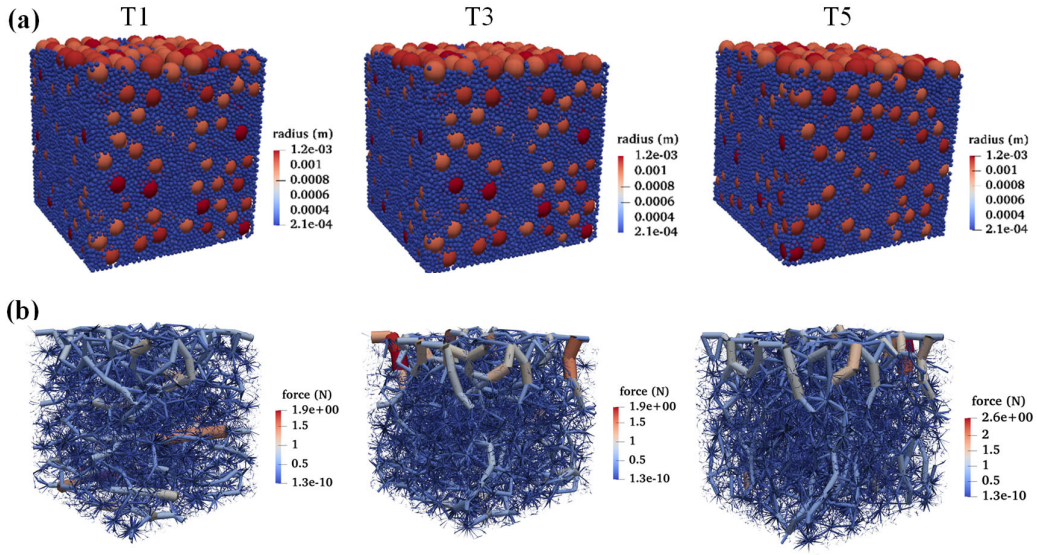


**Fig. 5** (a) Particle assemblies and (b) force chain networks of T1, T3 and T5 specimens before suffusion

The initial stress anisotropy of specimens T1 and T5 can be vividly seen from the distributions of contact normals and normal contact forces, as presented in rose diagrams in Fig. 6. For the T1 specimen, both the distributions of contact normals and normal contact forces prevail in the horizontal direction, in accordance with the direction of the major principal effective stress. The anisotropy intensity manifested by normal contact force distribution appears to be more distinct than that by contact normal distribution, as also observed in Yang et al. [63] and Hu et al. [28]. On the other hand, the T5 specimen exhibits the prevailing longitudinal distributions of contact normals and normal contact forces owing to its preferential vertical major effective stress. The drastic difference between specimens indicates that the anisotropic loading conditions result in significant variations of soil fabric even though both specimens have the same

void ratio. Correspondingly, the onset and development of suffusion is inevitably different, which will be elaborated in the following sections.

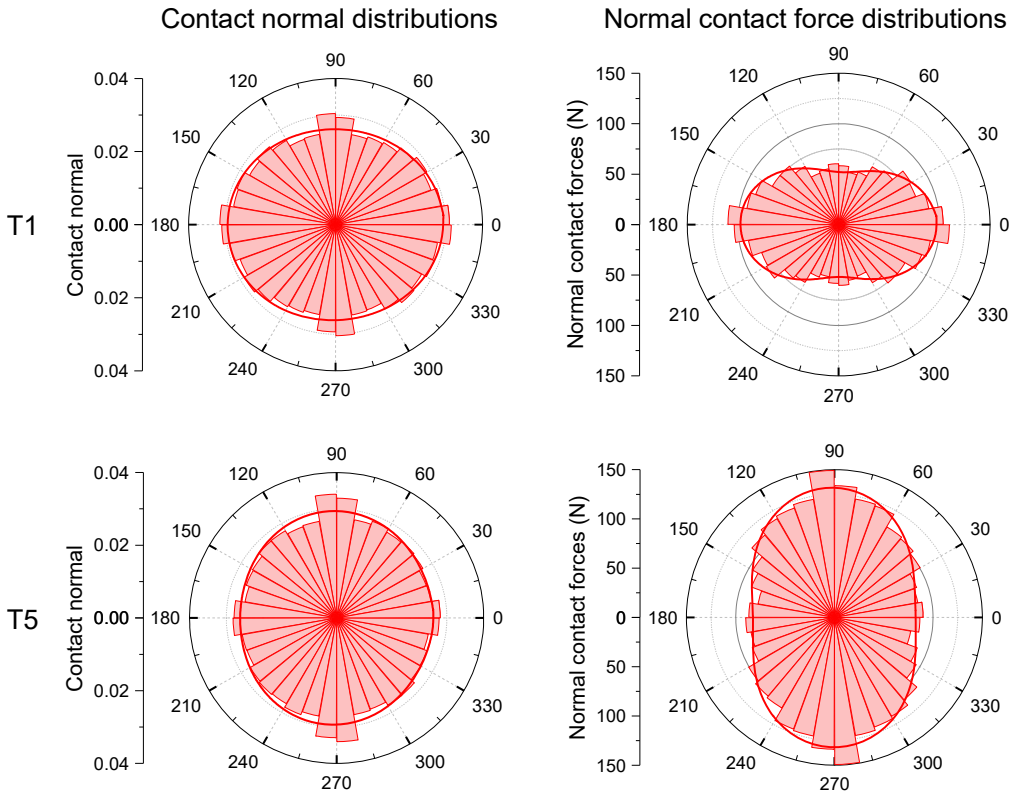


**Fig. 6** Distributions of contact normals and normal contact forces of the initially anisotropic non-eroded T1 and T5 specimens in a longitudinal plane

## 3.2 Results from suffusion stage

The evolutions of fines loss $\Delta FC$ by mass during suffusion for all specimens are illustrated in Fig. 7. It is seen that few fine particles are lost at low hydraulic gradient because the seepage force is insufficient to overcome the gravity and restrictions by neighboring particles on fine particles. With the increasing hydraulic gradient, fine particles start to get detached, migrate through the voids among coarse particles, and exit the permeable wall once the critical hydraulic gradient $i_{cr}$ is reached. The grain size distributions (GSDs) of specimens after the $t$ = 15s suffusion duration are plotted in Fig. 2. It is observed that the specimens with the major principal effective stress parallel to the primary seepage direction are the most erodible with the smallest critical hydraulic gradient and the greatest erosion rate. For example, suffusion triggers earliest at $t$ = 2.5s

and develops the maximum fines loss $\Delta FC$ = 10% at the end of suffusion for the T5 specimen ($\eta_0$ = 0.43), while the T3 specimen ($\eta_0$ = 0) exhibits the strongest suffusion resistance among others and its terminal fines loss is much smaller than that of T5 specimen (Fig. 7). The T1 specimen with the horizontal major principal effective stress exhibits the medium suffusion resistance. Comparison of the fines loss history between the T4 and T5 specimens as well as between the T1 and T2 specimens indicates that stress anisotropy promotes the onset and development of suffusion, regardless of the principal stress direction. This is consistent with the results of laboratory tests in Chang [66].

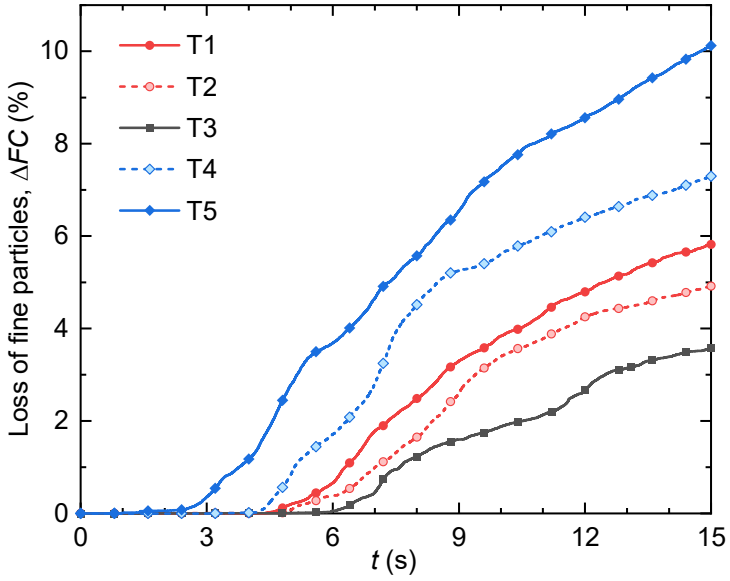


**Fig. 7** Evolution of fines loss $\Delta FC$ by mass with elapsed time for specimens under different initial stress anisotropy

To further investigate the detachment, migration and clogging of fine particles under suffusion, the soil specimen is vertically divided into six sections. The distributions of fine particles for specimens with different initial stress ratios, i.e., T1, T3 and T5 specimens, are illustrated in Fig. 8. Clearly, fine particles of non-eroded specimens are relatively uniformly distributed along all sections except the top section owing to the inevitable fines loss near the permeable top boundary during the reconsolidation process, as evidenced by Fig. 5. In addition, the fines loss $\Delta FC$ gradually increases from

279 the bottom to the top boundaries, and the top section exhibits the most severe fines loss
280 $\Delta FC$. This could be attributed to the formation of the repetitive clogging-unclogging
281 effect for the longer erosion path of fine particles in lower sections. Among all
282 specimens, the anisotropic T5 specimen exhibits the maximum fines loss at all sections,
283 while the isotropic T3 specimen exhibits the minimum fines loss compared with the
284 others (consistent with Fig. 7). Similar heterogeneous distributions of fine particles
285 were also reported in laboratory tests [17, 43] and other numerical studies [38, 67].

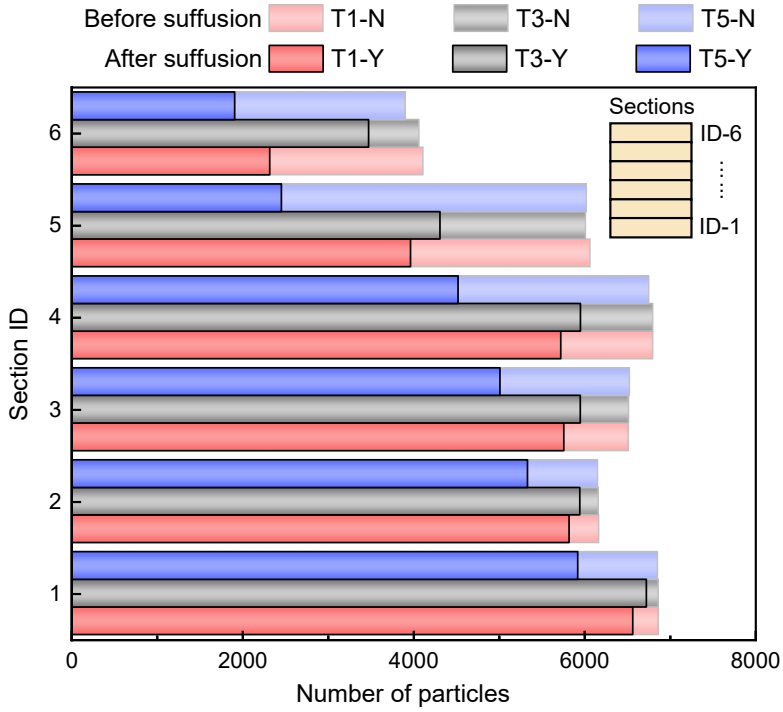


286

287 **Fig. 8** Distributions of fine particles along the longitudinal direction for the T1, T3, and T5
288 specimens. N - before suffusion; Y - after suffusion.

289 The evolutions of the volumetric deformation during suffusion are illustrated in Fig. 9
290 in terms of void ratio $e$, volumetric strain $\varepsilon_v$, axial strain $\varepsilon_a$ and horizontal strain $\varepsilon_h$.
291 Contraction is treated as positive following the sign convention in soil mechanics.
292 Under low hydraulic gradient, the combined effect of seepage flow disturbance and
293 confinement of boundary walls results in a slight volumetric contraction and decrease
294 of void ratio of all specimens (Fig. 9a and b). Once reaching the critical hydraulic
295 gradient $i_{cr}$, fine particles start to be detached and eroded out of the specimen, leading

296 to significant microstructural change and volumetric contraction. Because of the even
297 more rapid loss of fines and thus solid fraction in this period, the void ratio turns out to
298 be increasing during the apparent volumetric contraction. The turning point of void ratio
299 evolution from decrease to increase shows good agreement with the onset of suffusion
300 in Fig. 7. At the end of suffusion, all eroded specimens exhibit increased void ratio and
301 reduced volume compared to the non-eroded specimens, especially for the specimens
302 with larger initial stress anisotropy, i.e., T1 and T5 (Fig. 9a and b). The specimen with
303 the major principal effective stress aligned with the primary seepage direction (i.e., T5)
304 exhibits the most severe void ratio and volumetric changes which can be reasonably
305 attributed to the large fines loss (Fig. 7).

306 To further inspect the deformation patterns of different specimens during suffusion, the
307 evolutions of axial and horizontal strains are presented (Fig. 9c and d). It is seen that,
308 for the T4 and T5 specimens with initial triaxial compression, the volumetric
309 contraction in Fig. 9b is mainly caused by the positive axial strain of the soil matrix.
310 Conversely, for the T1 and T2 specimens with initial triaxial extension, the positive
311 horizontal strain is responsible for the volumetric contraction. The T3 isotropic
312 specimen exhibits the smallest axial, horizontal and volumetric strains compared with
313 the other scenarios. It is noted that the magnitudes of axial strain for all specimens are
314 approximately 2 ~ 3 times of those of horizontal strain, implying that suffusion results
315 in greater deformation along the direction of seepage flow, which is in agreement with
316 the previous laboratory suffusion tests [17, 43] and simulation results [42, 67]. The
317 different deformation features of specimens also indicated that the volumetric
318 deformation and microstructural changes under suffusion could be closely related to the
319 initial stress states of specimens, and thus results in different mechanical responses
320 under triaxial shearing, which will be discussed in the following section.

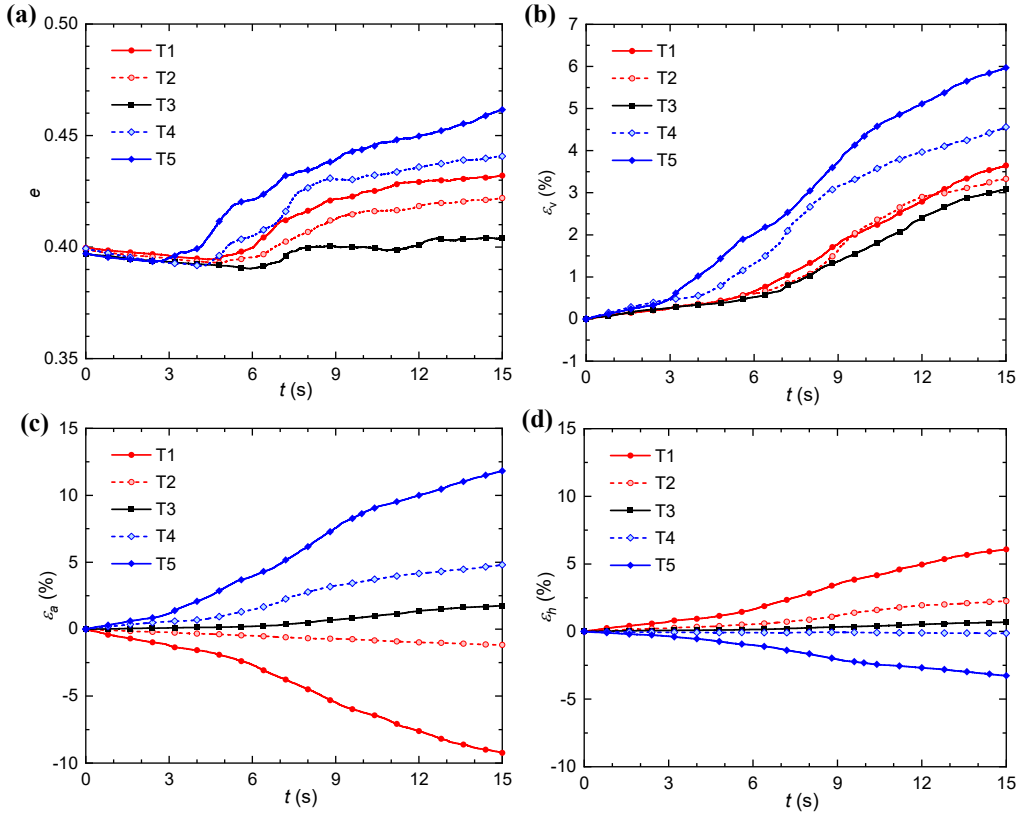


**Fig. 9** Evolutions of (a) void ratio $e$, (b) volumetric strain $\varepsilon_v$, (c) axial strain $\varepsilon_a$ and (d) horizontal strain $\varepsilon_h$ with the elapsed time of all specimens

## 3.3 Results from triaxial shear stage

Fig. 10 shows stress-strain curves of eroded and non-eroded specimens under drained triaxial conditions. Triaxial compression tests are performed on T4 and T5 specimens, and extension tests are performed on the T1 and T2 specimens. The isotropic T3 specimen is sheared under both triaxial compression and extension conditions. All simulation cases for triaxial shearing marked with designated specimen IDs are listed in Table 4. The results of the triaxial extension tests in Fig. 10a indicate that, the peak deviatoric stress $q$ of the eroded specimens is smaller than that of the non-eroded specimens, while the variations of the deviatoric stress sheared to large strain levels (approaching critical state) are negligible. The eroded soil specimens exhibit less volumetric dilatancy compared to the non-eroded specimens (Fig. 10b). Similar trend

is also observed for the specimens under triaxial compression conditions in Fig. 10c and d. Our observations agree well with the results of previous experimental studies [17, 43, 68, 69]. Noticing that suffusion is still developing at the end of the simulation at $t$ = 15s (Fig. 9) and there still exists a large portion of fine particles inside the specimens (Fig. 8), we expect that the reduction of peak shear strength and dilatancy will be more prominent given extended suffusion duration [13].

**Table 4** Simulation cases for triaxial compression and extension tests

| Specimen ID | Suffusion condition | Shear condition | Initial stress ratio, $\eta_0$ | Peak deviatoric stress, $q_{max}$ (kPa) | Secant modulus, $E_{50}$ (kPa) | Peak friction angle, $\varphi_p$ (°) | Residual friction angle, $\varphi_r$ (°) |
|---|---|---|---|---|---|---|---|
| T1-E-N | No | TE | -0.43 | 74.7 | 88.8 | 36.4 | 16.4 |
| T1-E-Y | Yes | TE | -0.43 | 71.8 | 59.0 | 34.1 | 15.5 |
| T2-E-N | No | TE | -0.23 | 72.8 | 120.7 | 34.8 | 15.8 |
| T2-E-Y | Yes | TE | -0.23 | 69.4 | 79.2 | 32.2 | 15.5 |
| T3-E-N | No | TE | 0 | 73.1 | 147.5 | 35.0 | 16.6 |
| T3-E-Y | Yes | TE | 0 | 69.5 | 106.6 | 32.2 | 16.5 |
| T3-C-N | No | TC | 0 | 239.3 | 284.6 | 32.9 | 13.1 |
| T3-C-Y | Yes | TC | 0 | 211.1 | 256.8 | 30.8 | 14.3 |
| T4-C-N | No | TC | 0.23 | 239.9 | 278.9 | 32.9 | 13.2 |
| T4-C-Y | Yes | TC | 0.23 | 215.4 | 237.6 | 31.1 | 16.5 |
| T5-C-N | No | TC | 0.43 | 245.1 | 274.2 | 33.3 | 14.1 |
| T5-C-Y | Yes | TC | 0.43 | 222.0 | 211.9 | 31.5 | 16.8 |

Yes = eroded; No = non-eroded; TE = triaxial extension shear; TC = triaxial compression shear.

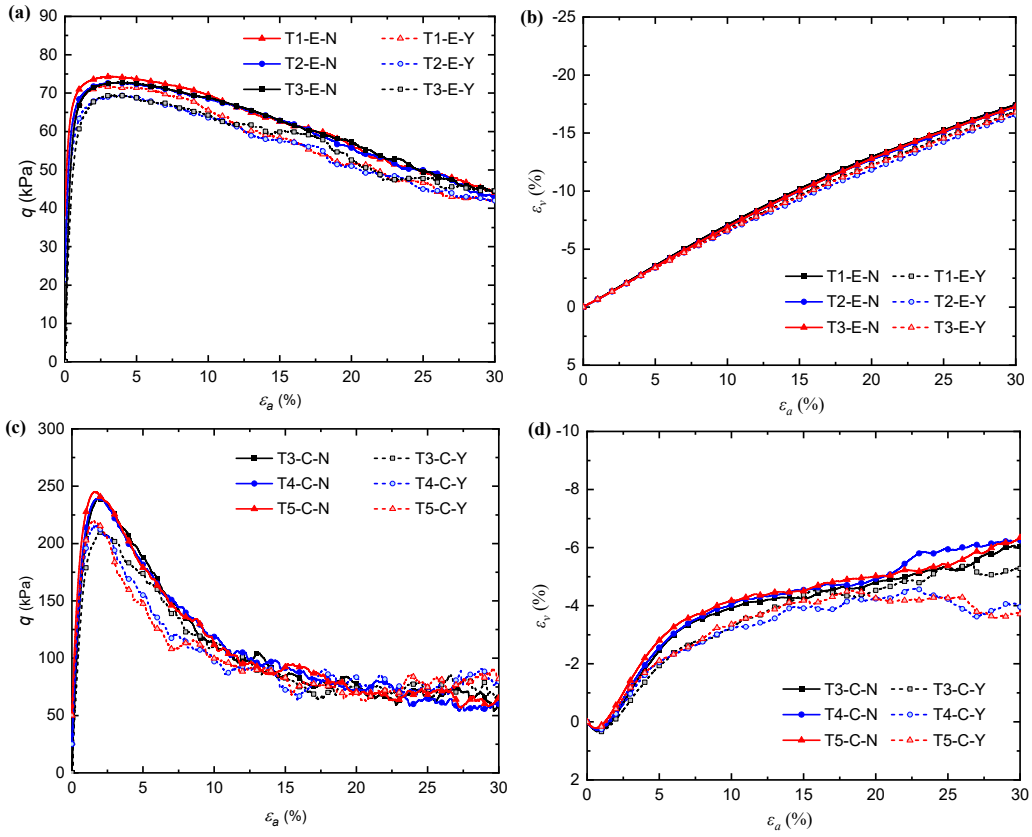


**Fig. 10** Evolutions of deviatoric stress $q$ and volumetric strain $\varepsilon_v$ versus axial strain $\varepsilon_a$ before and after suffusion under (a-b) triaxial extension tests (T1 ~ T3 specimens) and (c-d) triaxial compression tests (T1 ~ T3 specimens)

The shear stiffness of soils at small strain is also an important feature and is extensively concerned in engineering practice. Herein, a secant modulus corresponding to half of the peak shear stress, i.e., $E_{50}$, is introduced in Fig. 11 to evaluate the evolution of shear stiffness of soils under suffusion [70]. It is observed that the secant modulus $E_{50}$ under triaxial compression conditions is much greater than that under triaxial extension; for example, the $E_{50}$ in the T3-C is approximately twofold of that in the T3-E for both non-eroded and eroded specimens. Specimens with stronger initial stress anisotropy exhibit lower $E_{50}$ for triaxial extension specimens, but the trend is not obvious for triaxial compression specimens. Finally, erosion consistently reduces the $E_{50}$ of all specimens regardless of their initial stress state. This weakening effect can have important implications on the performance of water dams, e.g., promoting settlement and creep of the structure under sustained seepage.

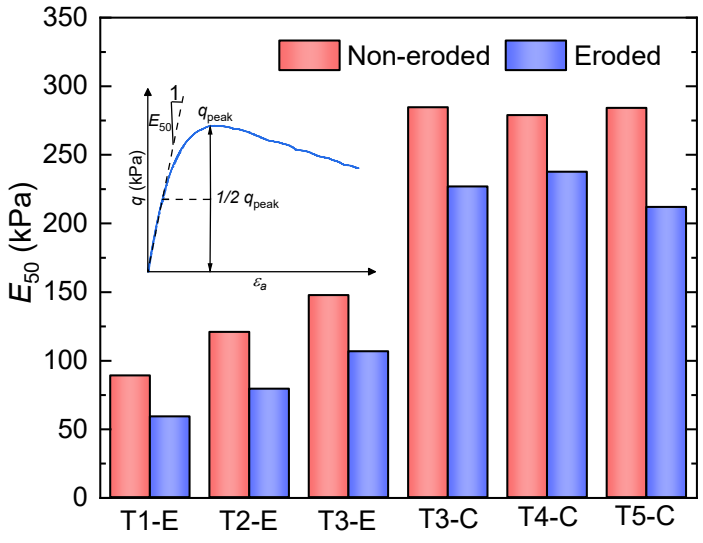


**Fig. 11** The secant modulus $E_{50}$ for all non-eroded and eroded specimens under triaxial shear

# 4. Microscopic inspections

## 4.1. Microscopic features during suffusion

The interparticle connectivity is one of the key features representing the microstructures of granular soils. Fig. 12 illustrates the evolutions of the coordination numbers of all specimens during suffusion, where the coordination number $Z$ denotes the average number of contacts per particle, and the mechanical coordination number $Z_m$ refers to the average number of contacts per active particle with two or more contacts [71, 72], calculated by:

$$Z = \frac{2C}{N} \tag{1}$$

$$Z_m = \frac{2C - N_1}{N - N_0 - N_1} \tag{2}$$

where $C$ is the total contact number; $N$ is the total particle number; $N_0$ and $N_1$ are the numbers of particles with null and only one contact (also called "rattlers"), respectively. When a granular system does not contain rattlers, one can see Eq. (2) becomes identical

to Eq. (1). Thus the difference between the values of $Z$ and $Z_m$ indirectly indicates the number of inactive fine particles floating inside the soil matrix. Since the large number of fine particles and their relatively inactive roles in force transmission inside the tested gap-graded soils, both the values of $Z$ and $Z_m$ are relatively low. This is consistent with the other DEM studies on gap-graded soils, e.g., Langroudi et al. [73] and Ahmadi et al. [74]. The isotropic T3 specimen has the maximum $Z$ and $Z_m$ during the full suffusion process, while the specimens with stronger initial stress anisotropy exhibit the lower $Z_m$ values. This indicates that the initial stress anisotropy weakens the connectivity among particles. In addition, it is seen from Fig. 12a that the variations of coordination number $Z$ are insignificant but exhibit severe fluctuation during suffusion, which could be attributed to intermittent clogging and unclogging during the migration of fine particles. On the contrary, Fig. 12b shows that the mechanical coordination number of all specimens $Z_m$ first increases smoothly due to the increased seepage force before the onset of suffusion (Fig. 9b), and then turns to decrease with the progressive detachment and migration of fine particles. The decreasing trend of $Z_m$ indicates that some active particles formerly participating in sustaining external forces are eroded under suffusion. It is also interesting to note that, although all specimens have distinct initial stress states, the mechanical coordination number $Z_m$ tends to reach the same value for the specimens with the same absolute values of stress ratio at the end of suffusion regardless of the incipient major principal stress direction (Fig. 12b). The decreasing $Z_m$ values of all specimens explain why the secant modulus $E_{50}$ and the peak shear strength are weakened at the end of suffusion (Figs. 10 and 11).

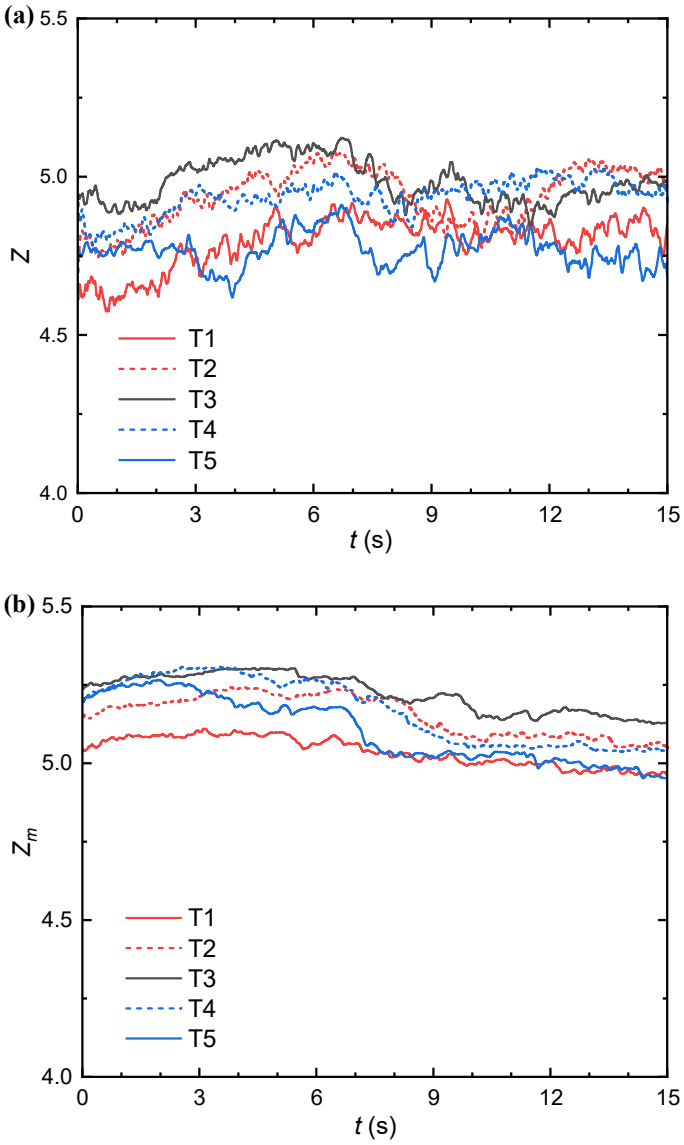


**Fig. 12** Evolutions of (a) coordination numbers $Z$ and (b) mechanical coordination numbers $Z_m$ with the elapsed time of all specimens

It is well understood that the roles of coarse and fine particles in force transmission are different for gap-graded specimens. Herein, the coordination numbers of different contact types are further examined, including the contacts between two coarse particles (*C*-*C* contact), those between a coarse and fine particle (*C*-*F* contact), and those between two fine particles (*F*-*F* contact). Correspondingly, three coordination numbers are defined as the average numbers of *C*-*C* contacts per coarse particle $Z_{C\text{-}C}$, *C*-*F* contacts per coarse particle $Z_{C\text{-}F}$ and *F*-*F* contacts per fine particle $Z_{F\text{-}F}$, respectively.

The evolutions of the three coordination numbers during suffusion are presented in Fig. 13. It is observed that, $Z_{C\text{-}C}$ gradually increases yet $Z_{C\text{-}F}$ decreases with elapsed time for all specimens. This indicates that the detachments of fine particles mainly cause the breakup of *C*-*F* contacts, and in turn enhance the connectivity of *C*-*C* contacts. The distribution of fine particles inside the voids among coarse particles maintains stable, as evidenced by the overall constant $Z_{F\text{-}F}$ values for all cases throughout suffusion. Given that the loss of fine particles during suffusion would inevitably reduce the coordination number between fine particles, the overall constant $Z_{F\text{-}F}$ implies that the decrease of contacts is somehow compensated by the local concentration of fine particles and *F*-*F* contacts under the restrictions of the soil skeleton, which could be seen as evidence of the clogging phenomenon during suffusion. Comparison of different specimens indicates that the changes of $Z_{C\text{-}C}$ and $Z_{C\text{-}F}$ are more severe for the specimens with higher initial stress anisotropy, especially for the specimens under initial triaxial compression (T4 and T5). Conversely, the isotropic T3 specimen has much smaller variations of $Z_{C\text{-}C}$ and $Z_{C\text{-}F}$ and is less disturbed by suffusion, which is in accordance with the least fines loss and the smallest volumetric deformation during suffusion (Figs. 7 and 9).

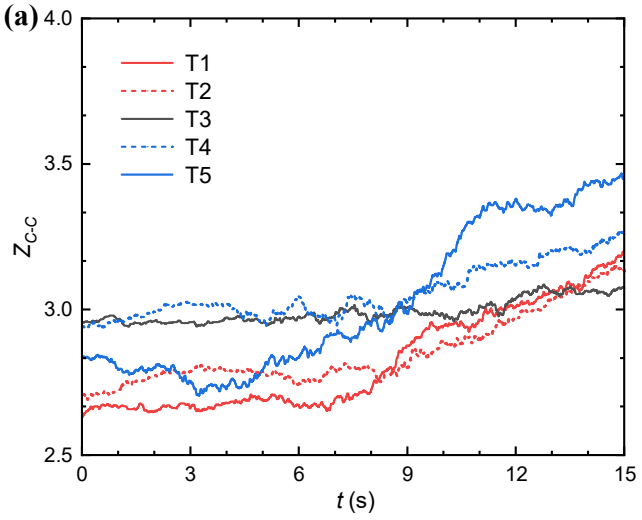

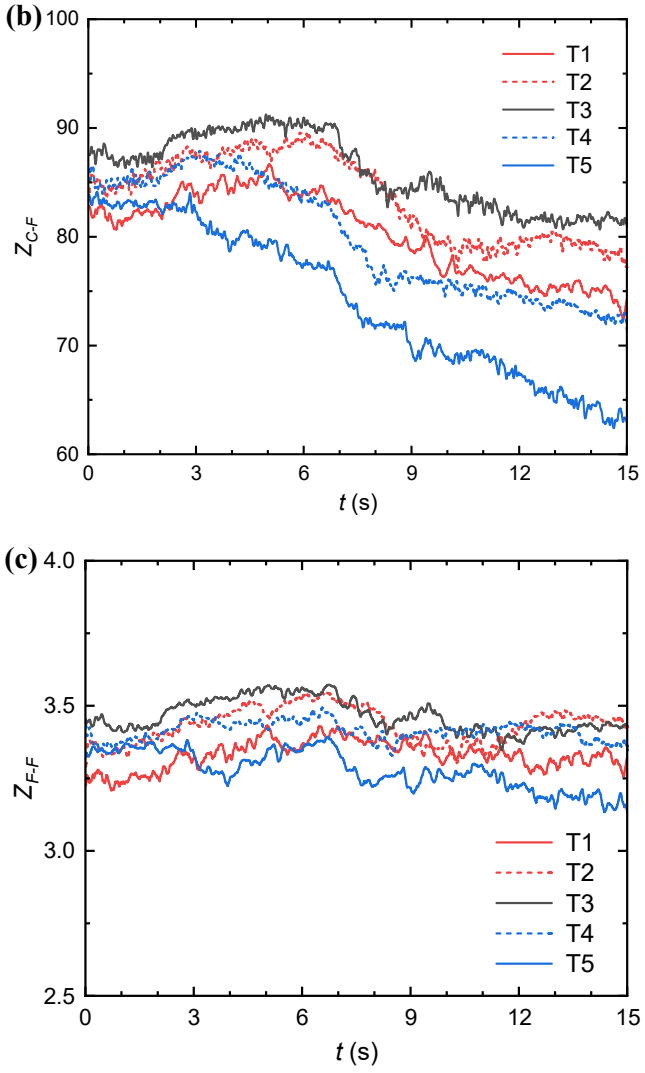


425

426

427 **Fig. 13** Evolutions of coordination numbers of all specimens during suffusion in terms of: (a) $Z_{C\text{-}C}$;

428 (b) $Z_{C\text{-}F}$ and (c) $Z_{F\text{-}F}$

429 To further analyze the evolution of contact force chains of specimens during suffusion,

430 the interparticle contacts are divided into strong and weak contacts, where the contact

431 forces greater than the average contact force $\overline{f_n}$ form the strong contact force chain,

432 and the others form the weak contact force chain [72, 75]. Fig. 14 exhibits the evolution

433 of the proportion of weak contact forces during suffusion for all specimens, calculated

434 by the sum of the absolute value of the weak contact forces $f_n^w$ divided by that of the

435 normal contact forces $f_n$. It is observed that all cases exhibit the similar evolution trend

436 with a temporary increase followed by a rapid decrease period. The first increase period

indicates that, particles gain more contacts with each other and sustain weak contact forces at the initial stage. However, these weak contacts are relatively fragile and are easily disrupted under seepage effect, resulting in the following rapid decrease of the proportion of weak contact forces. Note that the T5 specimen exhibits the greatest $f_n^w/f_n$ at the initial state, while it evolves to the lowest value at the end of suffusion. This indicates that a large number of particles of the T5 specimen are initially inactive or in weak contacts with the neighbors, and thus suffusion can be more easily triggered, as evidenced by the severe decrease of weak contact forces with suffusion (Fig. 14). The greater initial stress anisotropy exhibits the more severe falls of $f_n^w/f_n$ at the end of suffusion, especially for the specimens under initial triaxial compression (T5). The isotropic T3 specimen is found to be the most stable with the smallest fall of $f_n^w/f_n$.

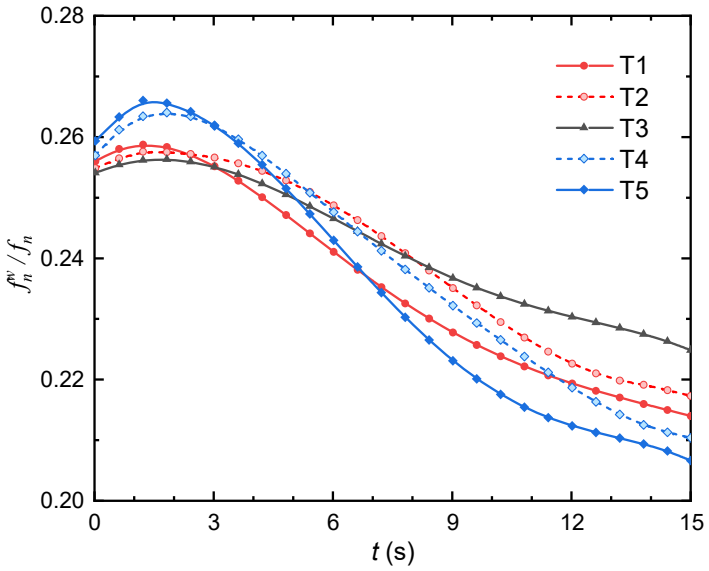


**Fig. 14** Evolutions of the proportion of weak contacts during suffusion for all specimens

## 4.2. Microscopic characteristics during shearing

The evolutions of coordination numbers during triaxial compression and extension tests are presented in Fig. 15. It is seen that the particles inside the original non-eroded specimens are in good contact with each other, as evidenced by approximately the same $Z$ and $Z_m$ values at the initial state ($\varepsilon_a = 0$). With the development of shearing, both $Z$

and $Z_m$ continuously decrease, and the difference between $Z$ and $Z_m$ becomes larger for both triaxial extension (Fig. 15a-b) and compression (Fig. 15c-d) conditions. This indicates that some particles formerly actively participating in force transmission gradually evolve to inactive particles with null or one contact during shearing. Furthermore, comparison between the coordination numbers of non-eroded and eroded specimens under triaxial extension conditions indicates that, the coordination numbers $Z$ of eroded specimens are generally smaller than those of non-eroded specimens (Fig. 15a), while their difference in the mechanical coordination numbers $Z_m$ is negligible (Fig. 15b). This implies that there exists a greater and increasing portion of inactive fine particles in eroded specimens during shearing. The detached yet remaining fine particles under suffusion are mostly inactive in force transmission. The same observation is also found in triaxial compression conditions (Fig. 15c-d). This helps explain the insignificant variation of shear strength of soil specimens at large strain levels. It is also interesting to note that at the end of shearing, both $Z$ and $Z_m$ tend to approach their corresponding steady-state values, depending only on the GSDs of specimens and the shear conditions, which is in agreement with Jiang et al. [71] and Hu et al. [28].

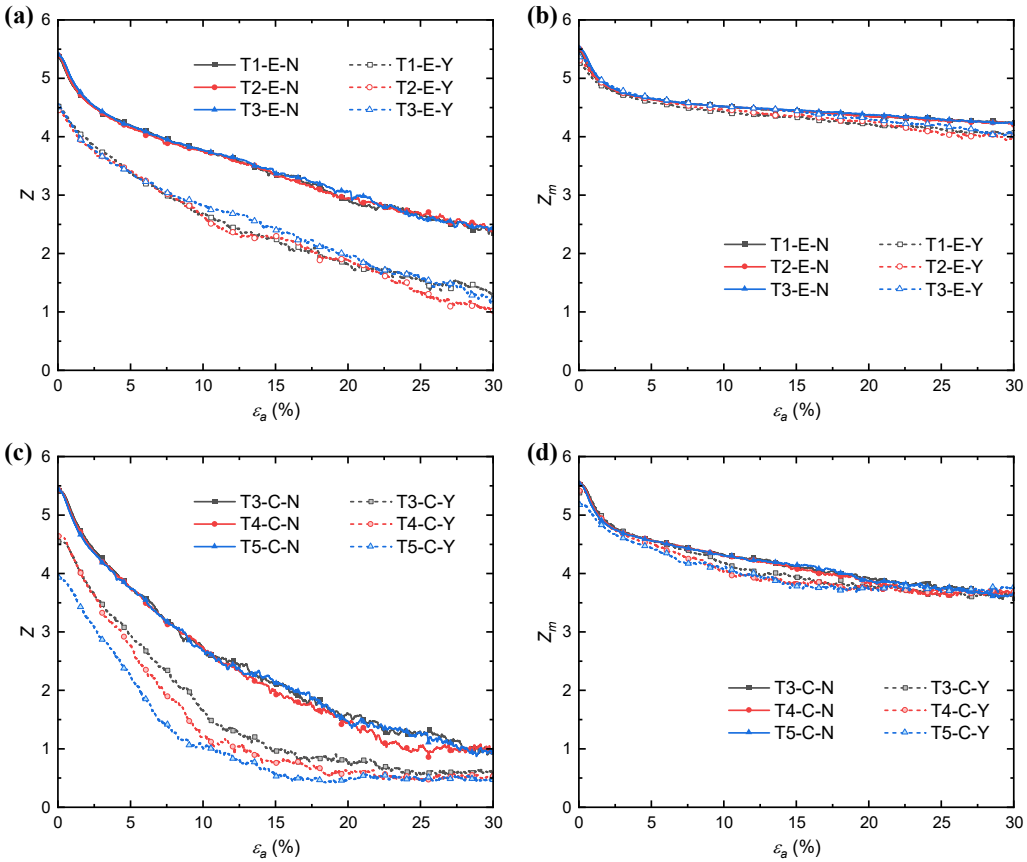


**Fig. 15** Evolutions of (mechanical) coordination numbers: (a) $Z$ and (b) $Z_m$ during triaxial extension tests, and (c) $Z$ and (d) $Z_m$ during triaxial compression tests

The evolutions of coordination numbers of different contact types, i.e., $Z_{C\text{-}C}$, $Z_{C\text{-}F}$, and $Z_{F\text{-}F}$, during shearing are illustrated in Fig. 16. It is seen that, although the $Z$ and $Z_m$ of eroded specimens converge to the same values under the same shear conditions (Fig. 15), their coordination numbers with respect to different contact types are diverse. For the triaxial extension conditions, it is found that the $Z_{C\text{-}C}$ values of the eroded specimens are relatively higher, yet their $Z_{C\text{-}F}$ and $Z_{F\text{-}F}$ values are much lower than those of the non-eroded specimens (Fig. 16a-c). This indicates that suffusion results in the more active participation of coarse particles in force transmission during shearing, while the connectivity of fine particles with the neighbors is weakened, as manifested by the reduced $Z_{C\text{-}F}$ and $Z_{F\text{-}F}$ values. The same observation is also found in the triaxial compression conditions (Fig. 16d-e). The coordination number evolutions for triaxial compression specimens are more distinct from each other. For example, the T5

specimen with the greatest initial stress anisotropy exhibits the highest $Z_{C\text{-}C}$ value but the lowest $Z_{C\text{-}F}$ and $Z_{F\text{-}F}$ values throughout the shearing process. The lower $Z$ value of eroded T5 specimen during shearing in Fig. 15c is mainly caused by the poor connectivity of fine particles with the neighbors, i.e., the lower $Z_{C\text{-}F}$ and $Z_{F\text{-}F}$ values (Fig. 16e-f), which is likely responsible for the reduced secant modulus and shear strength of the eroded T5 specimen.

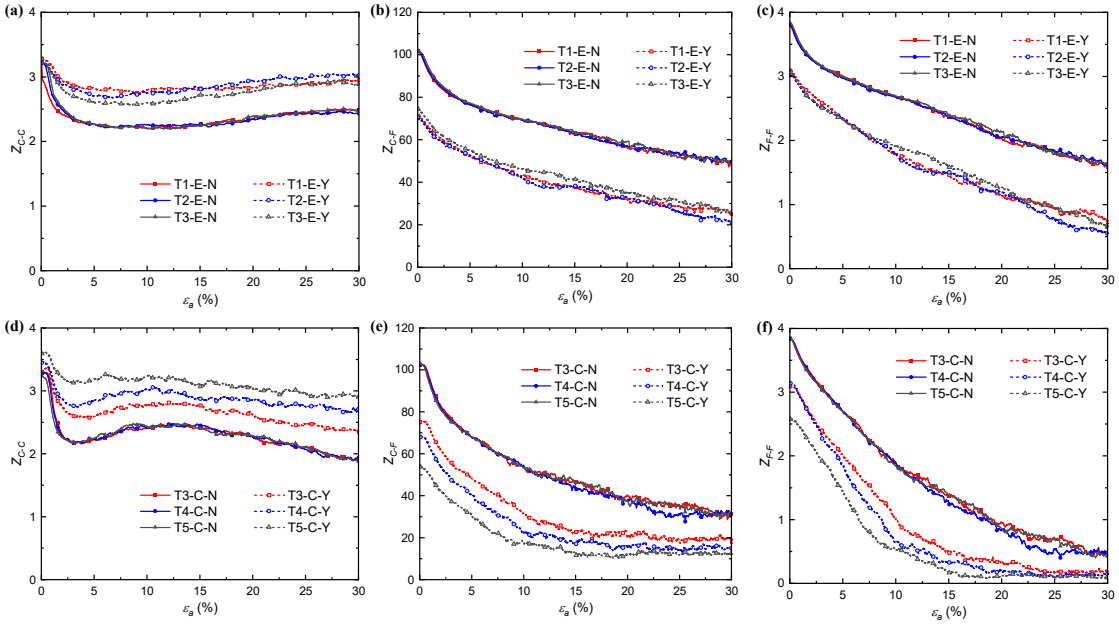


**Fig. 16** Evolutions of coordination numbers: (a) $Z_{C\text{-}C}$ , (b) $Z_{C\text{-}F}$ , and (c) $Z_{F\text{-}F}$ under triaxial extension, and (d) $Z_{C\text{-}C}$ , (e) $Z_{C\text{-}F}$ , and (f) $Z_{F\text{-}F}$ under triaxial compression conditions

## 4.3. Evolutions of fabric anisotropy during suffusion and shearing

It is widely recognized that fabric anisotropy could significantly affect the mechanical responses of granular soils [76, 77]. Two sources of fabric anisotropy are normally adopted, i.e., the geometrical and the mechanical anisotropy. The geometrical anisotropy stems from the distribution of contact normals and particle orientations, and the mechanical anisotropy is mainly caused by the distribution of normal contact forces [13, 78]. Given the significant stress anisotropy of the specimens in this study, the mechanical anisotropy [48, 79] is adopted for evaluating the fabric structure of the specimens:

$$\chi_{ij}^{n} = \frac{1}{N}\sum_{c\in N}\frac{f^{n}n_{i}n_{j}}{1+a_{kl}^{c}n_{k}n_{l}} \tag{3}$$

where $f^n$ is the absolute value of normal contact force; $n_i$ is the unit vector along the contact normal direction; $a_{ij}^{c}$ is deviatoric and symmetric and characterizes the fabric anisotropy, calculated as:

$$\phi_{ij} = \frac{1}{N}\sum_{c\in N} n_{i}n_{j} \tag{4}$$

$$a_{ij}^{c} = \frac{15}{2}\phi'_{ij} \tag{5}$$

where $\phi_{ij}$ is the contact normal fabric tensor and $\phi'_{ij}$ is the deviatoric part of $\phi_{ij}$. Herein, the normal-contact-force anisotropy tensor $a^n$ is defined as:

$$a_{ij}^{n} = \frac{15}{2}\frac{\chi'^{n}_{ij}}{\overline{f}^{0}} \tag{6}$$

where $\chi'^{n}_{ij}$ is the deviatoric part of $\chi_{ij}^{n}$, $\overline{f}^{0} = \chi_{ii}^{n}$ is the average normal force. The deviatoric invariant of $a^n$ is adopted to quantify the degree of mechanical anisotropy caused by normal contact forces:

$$a_{n} = \sqrt{\frac{3}{2}a_{ij}^{n}} \tag{7}$$

Fig. 17 presents the evolution of normal-contact-force anisotropy $a_n$ of specimens during suffusion and shearing. It is observed that suffusion has almost no contribution to the fabric anisotropy of specimens, except for the T5 specimen with the strongest initial stress anisotropy and the most severe fines loss, which exhibits a slight increase of $a_n$ with elapsed time (Fig. 17a). The difference of initial $a_n$ values between different specimens is mainly caused by the initial stress anisotropy before suffusion. Comparing the suffusion-induced fabric anisotropy, the triaxial shearing results in the more distinct fabric anisotropy in terms of normal contact forces (Fig. 18b and c). The fabric anisotropy $a_n$ peaks and reaches the corresponding stable states at the same strain level as the deviatoric stress $q$ (Fig. 10), which is coincident with the other DEM researches, e.g., Guo and Zhao [48] and Zhao and Kruyt [80]. Note that the difference of $a_n$ between

the eroded and noneroded specimens is relatively small, which also implies the suffusion-induced fines loss in gap-graded soils may not result in significant variation of force chain networks.

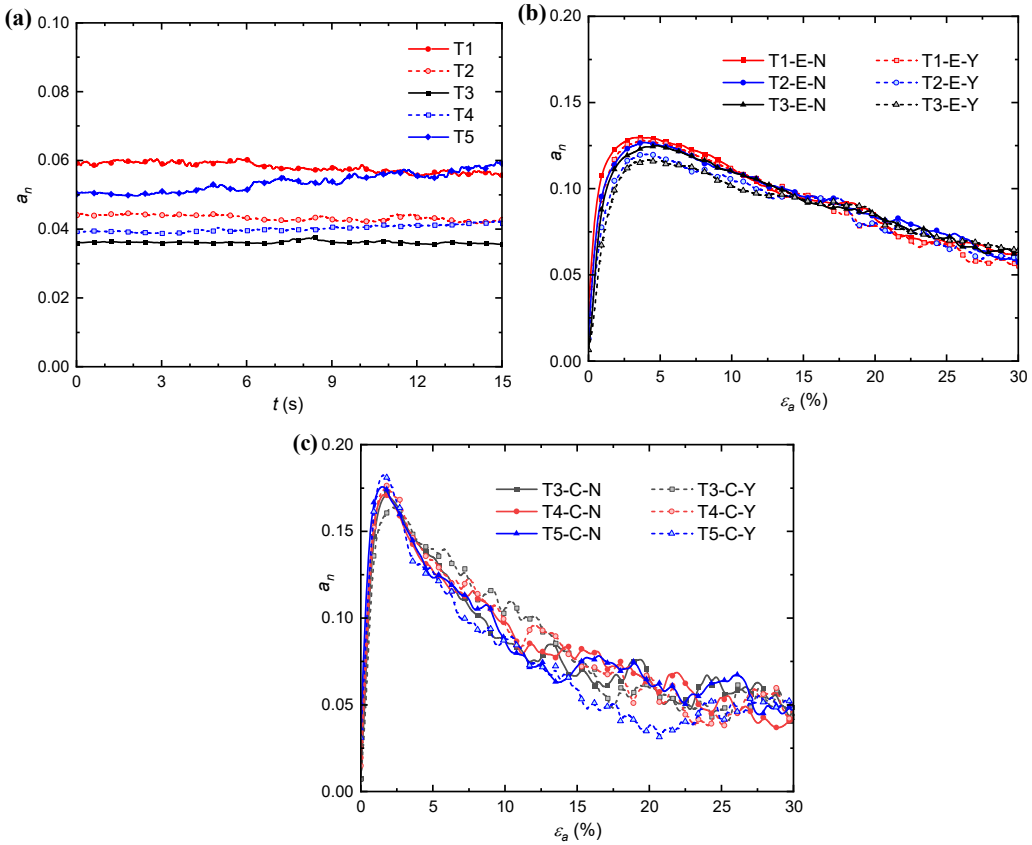


**Fig. 17** Evolutions of normal-contact-force anisotropy $a_n$ during (a) suffusion, (b) triaxial compression, and (c) triaxial extension tests

To further investigate the contribution of different contact types to stress anisotropy, Fig. 18 presents the distributions of strong normal contact forces $f_n^s$ and weak normal contact forces $f_n^w$ in a longitudinal plane before suffusion by means of rose diagrams. It shows that the preferential direction of the strong normal contact force distribution is generally consistent with the major principal stress direction, and the stress anisotropy enlarges with the initial stress ratio. However, the stress anisotropy with respect to weak contact forces is rather insignificant. This indicates that external forces are mainly sustained by the strong contact force chain, and thus the variation of stress ratio merely results in the anisotropic distribution of strong normal contact forces. Conversely, the weak contact force chain is insensitive to stress variation, and thus exhibits only a small

546 degree of anisotropy compared with the strong contact force chain. Note that in severely
547 gap-graded soils, the majority of strong normal contact forces are commonly sustained
548 by coarse particles in *C*-*C* contacts [28], while these contacts only occupy a small
549 portion of interparticle contacts of the soil matrix, as evidenced by the much greater $Z_{C\text{-}F}$
550 values than $Z_{C\text{-}C}$ values (Fig. 13b). The small degree of anisotropy of weak contact
551 forces is responsible for the insignificant global fabric anisotropy $a_n$ in Fig. 17a.

552 To be more specific, Fig. 19 presents the normal contact force distributions in a
553 longitudinal plane at different shear stages for the eroded T5 specimen with the
554 strongest initial stress anisotropy. Again, the distribution of strong contacts shows
555 distinct anisotropy manifested by the elliptical or peanut-shaped rose diagrams, while
556 the distribution of weak contacts maintains overall isotropic and evolves only slight
557 anisotropy at the peak shear state $\varepsilon_a$ = 2%. Furthermore, by dividing the interparticle
558 contacts into three types, i.e., *C*-*C*, *C*-*F* and *F*-*F* contacts, the distributions of normal
559 contact forces of different contact types are also presented. It is found that all these
560 contact types have a certain degree of initial normal-contact-force anisotropy which is
561 consistent with the initial stress state, and evolve more distinctly with the triaxial
562 shearing, especially at the peak shear state $\varepsilon_a$ = 2%. Among all contact types, the
563 normal-contact-force anisotropy of *C*-*C* and *C*-*F* contacts is significantly greater than
564 that of *F*-*F* contacts. This indicates that, coarse particles play the dominant role in strong
565 force transmission by *C*-*C* and *C*-*F* contacts, and only very few fine particles are
566 involved in forming strong force chain by *F*-*F* contact with the smaller $a_n$.

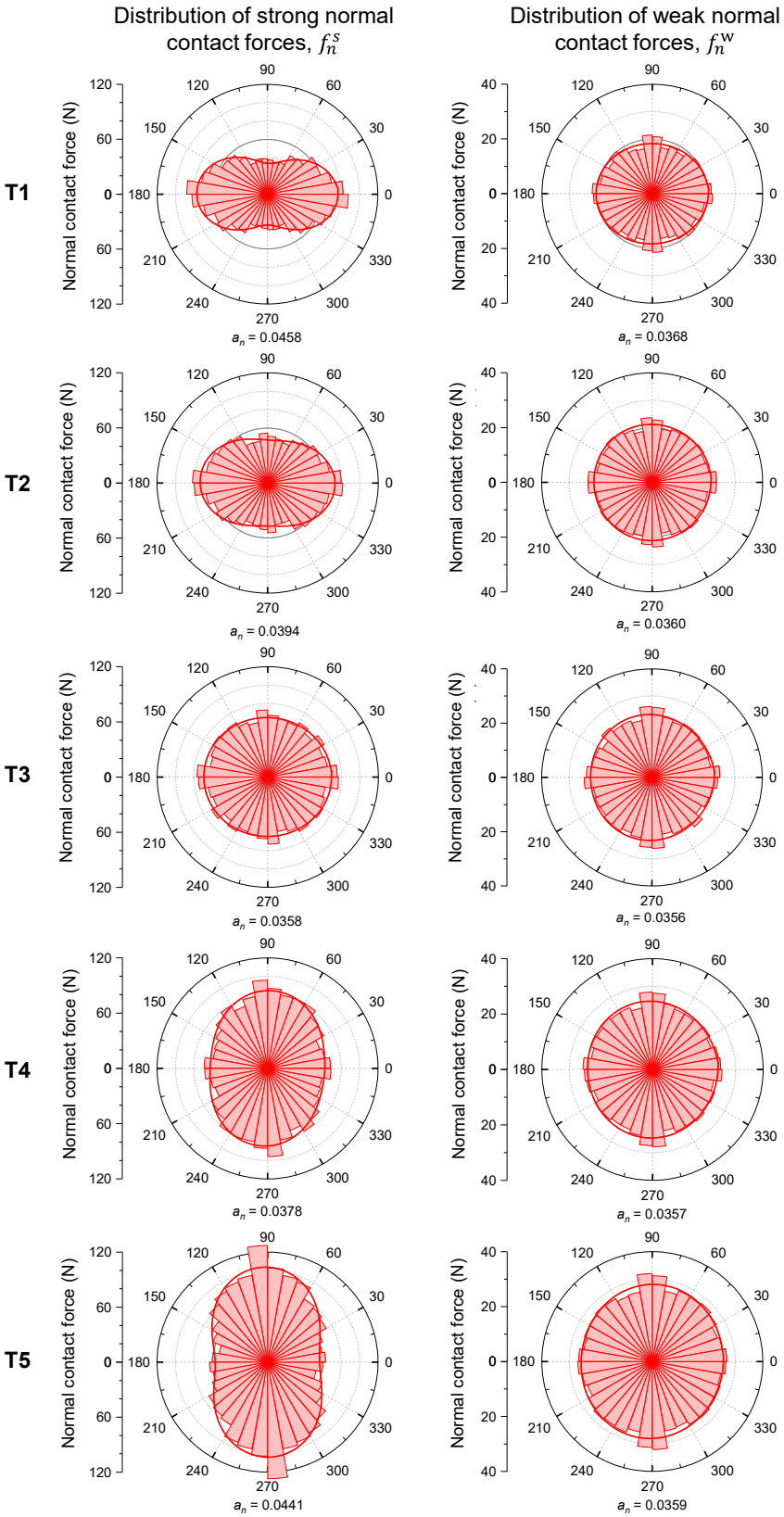


**Fig. 18** Distributions of strong and weak normal contact forces before suffusion

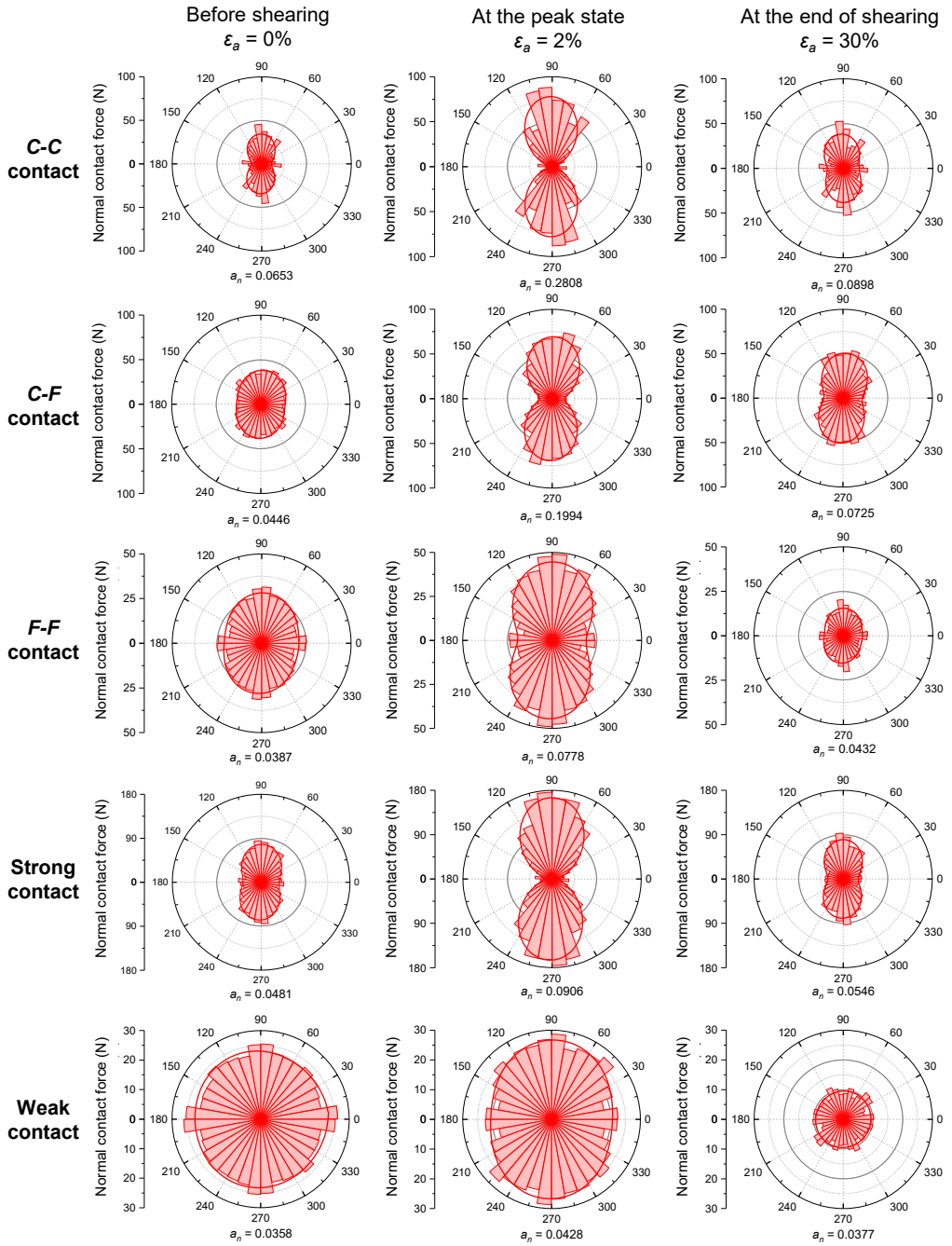


**Fig. 19** Distributions of normal contact forces of the eroded T5 specimen with the strongest initial stress anisotropy (ID: T5-C-Y) during triaxial compression test

## 5. Conclusions

This study presents a systematic CFD−DEM investigation on the influence of initial stress anisotropy on suffusion and shear behaviors of gap-graded soils. Several gap-graded specimens with different initial stress ratios are generated and then subjected to

suffusion and triaxial shearing. The contact statistics of both non-eroded and eroded specimens are monitored and analyzed to understand the micro-mechanisms of initial stress anisotropy on the suffusion and shear behaviors of soils. The main conclusions are summarized below:

1. Gap-graded specimens with the higher initial stress anisotropy and with the major principal stress aligned with the primary seepage direction are more prone to suffusion. Fines loss is positively correlated with the increase of volumetric contraction and void ratio.

2. The eroded specimens exhibit reduced peak deviatoric stress and volumetric dilation but have similar strain-softening behaviors compared to noneroded specimens under triaxial shearing. All specimens tend to evolve towards the same deviatoric stress when sheared to large strain levels regardless of experienced suffusion history. Suffusion also reduces the secant stiffness and peak friction angle of soils.

3. The initial stress anisotropy weakens the connectivity among particles, resulting in less force-transmitting contacts (reflected through the mechanical coordination number $Z_m$) during suffusion. Inactive fines loss under suffusion can cause reduced coarse-to-fine contacts and increased coarse-to-coarse contacts. The clogging-unclogging of fine particles is likely to cause severe fluctuation of the coordination number for fine-to-fine contacts $Z_{F\text{-}F}$ during suffusion.

4. The average and mechanical coordination numbers at the end of triaxial shearing appear to only depend on the soil GSD and the stress path and are independent of the initial stress anisotropy. During shearing, eroded specimens exhibit more active participation of coarse particles in force transmission through coarse-to-coarse contacts and less connectivity of fine particles with the neighbors.

5. The normal-contact-force anisotropy $a_n$ is found to enlarge with the initial stress ratio. The applied anisotropic stress is mainly carried by strong contacts governed by coarse-to-coarse contacts during suffusion and shearing. The abundant weak contacts in soil matrix are uniformly distributed with insignificant anisotropy. This is responsible for the overall constant $a_n$ during suffusion.

606 This study highlights that the initial stress anisotropy of the soil matrix has a profound
607 effect on the onset and development of suffusion, and thus can subsequently alter the
608 mechanical behaviors of eroded specimens. Future extensions of the present work
609 include examining the inherent fabric anisotropy caused by different particle shapes
610 and arrangements in natural soils and the effect of dynamic hydraulic conditions on
611 suffusion. The latter is highly relevant for the engineering of marine foundations and is
612 not well understood at the current moment.

613 ## Data Availability Statement

614 The datasets generated and analyzed during the current study are available from the
615 corresponding author upon reasonable request.

616 ## Acknowledgements

617 Z. Hu wishes to thank the support of the Natural Science Foundation of China (No.
618 52008409), the Basic and Applied Basic Research Foundation of Guangzhou (No.
619 202102020212), and the MOE Key Laboratory of Soft Soils and Environmental
620 Engineering, Zhejiang University (2020P01). Y. Zhang wishes to thank the support of
621 the University of Colorado Boulder through the startup funding.

622

# References


1. Muir Wood D (2007) The magic of sands — The 20th Bjerrum Lecture presented in Oslo, 25 November 2005. Can Geotech J 44:1329–1350
2. Xu Y, Zhang LM (2009) Breaching parameters for earth and rockfill dams. J Geotech Geoenviron Eng 135:1957–1970
3. Danka J, Zhang LM (2015) Dike failure mechanisms and breaching parameters. J Geotech Geoenviron Eng 141:04015039
4. Richards KS, Reddy KR (2012) Experimental investigation of initiation of backward erosion piping in soils. Géotechnique 62:933–942
5. Wan CF, Fell R (2008) Assessing the potential of internal instability and suffusion in embankment dams and their foundations. J Geotech Geoenviron Eng 134:401–407
6. Chang DS, Zhang LM (2013) Extended internal stability criteria for soils under seepage. Soils Found 53:569–583
7. Kawano K, Shire T, O'Sullivan C (2018) Coupled particle-fluid simulations of the initiation of suffusion. Soils Found 58:972–985
8. Maroof MA, Mahboubi A, Noorzad A (2021) Effects of grain morphology on suffusion susceptibility of cohesionless soils. Granul Matter 23:1–20
9. Chang DS, Zhang LM (2013) Critical hydraulic gradients of internal erosion under complex stress states. J Geotech Geoenviron Eng 139:1454–1467
10. Shire T, O'Sullivan C, Hanley KJ, Fannin RJ (2014) Fabric and effective stress distribution in internally unstable soils. J Geotech Geoenviron Eng 140:04014072
11. Liu Y, Wang L, Hong Y, et al (2020) A coupled CFD-DEM investigation of suffusion of gap graded soil: Coupling effect of confining pressure and fines content. Int J Numer Anal Methods Geomech 44:2473–2500
12. Moffat R, Fannin JR (2011) A hydromechanical relation governing internal stability of cohesionless soil. Can Geotech J 48:413–424
13. Hu Z, Yang ZX, Zhang YD (2020) CFD-DEM modeling of suffusion effect on undrained behavior of internally unstable soils. Comput Geotech 126:103692
14. Wang X, Huang B, Tang Y, et al (2022) Microscopic mechanism and analytical modeling of seepage-induced erosion in bimodal soils. Comput Geotech 141:104527
15. Yin Y, Cui Y, Tang Y, et al (2021) Solid–fluid sequentially coupled simulation of internal erosion of soils due to seepage. Granul Matter 23:1–14
16. Ma Q, Wautier A, Zhou W (2021) Microscopic mechanism of particle detachment in granular materials subjected to suffusion in anisotropic stress states. Acta Geotech 16:2575–2591
17. Chang DS, Zhang L (2011) A stress-controlled erosion apparatus for studying internal erosion in soils. Geotech Test J 34:579–589
18. Sterpi D (2003) Effects of the erosion and transport of fine particles due to seepage flow. Int J Geomech 3:111–122
19. Van Beek VM, Van Essen HM, Vandenboer K, Bezuijen A (2015) Developments in modelling of backward erosion piping. Géotechnique 65:740–754
20. Chen C, Zhang LM, Chang DS (2016) Stress-strain behavior of granular soils subjected to internal erosion. J Geotech Geoenviron Eng 142:06016014
21. Vardoulakis I, Stavropoulou M, Papanastasiou P (1996) Hydromechanical aspects of sand

production problem. Transp Porous Media 22:225–244
22. Cividini A, Gioda G (2004) Finite-element approach to the erosion and transport of fine particles in granular soils. Int J Geomech 4:191–198
23. Burman BC, Cundall PA, Strack ODL (1980) A discrete numerical model for granular assemblies. Géotechnique 30:331–336
24. Muir Wood D, Maeda K, Nukudani E (2010) Modelling mechanical consequences of erosion. Géotechnique 60:447–457
25. Scholtès L, Hicher PY, Sibille L (2010) Étude Par Approches Multi-Échelles De La Réponse Mécanique D'Un Milieu Granulaire Induite Par L'Extraction De Ses Particules. Comptes Rendus - Mec 338:627–638
26. Zhang F, Li M, Peng M, et al (2019) Three-dimensional DEM modeling of the stress–strain behavior for the gap-graded soils subjected to internal erosion. Acta Geotech 14:487–503
27. Hicher P-Y (2013) Modelling the impact of particle removal on granular material behaviour. Géotechnique 63:118–128
28. Hu Z, Zhang Y, Yang Z (2020) Suffusion-induced evolution of mechanical and microstructural properties of gap- graded soils using CFD-DEM. J Geotech Geoenviron Eng 146:1–18
29. Tao J, Tao H (2017) Factors affecting piping erosion resistance : revisited with a numerical modeling approach. Int J Geomech ASCE 17:1–14
30. Guo Y, Yu X (2017) Comparison of the implementation of three common types of coupled CFD-DEM model for simulating soil surface erosion. Int J Multiph Flow 91:89–100
31. Cheng K, Wang Y, Yang Q (2018) A semi-resolved CFD-DEM model for seepage-induced fine particle migration in gap-graded soils. Comput Geotech 100:30–51
32. Yang Q, Cheng K, Wang Y, Ahmad M (2019) Improvement of semi-resolved CFD-DEM model for seepage-induced fine-particle migration: Eliminate limitation on mesh refinement. Comput Geotech 110:1–18
33. Tsuji Y, Kawaguchi T, Tanaka T (1993) Discrete particle simulation of two-dimensional fluidized bed. Powder Technol 77:79–87
34. Zhou ZY, Kuang SB, Chu KW, Yu AB (2010) Discrete particle simulation of particle-fluid flow: Model formulations and their applicability. J Fluid Mech 661:482–510
35. Kloss C, Goniva C, Hager A, et al (2012) Models, algorithms and validation for opensource DEM and CFD-DEM. Prog Comput Fluid Dyn An Int J 12:140
36. Tao H, Tao J (2017) Quantitative analysis of piping erosion micro-mechanisms with coupled CFD and DEM method. Acta Geotech 12:573–592
37. Mu L, Zhang P, Shi Z, Huang M (2022) Computers and Geotechnics Coupled CFD – DEM Investigation of Erosion Accompanied by Clogging Mechanism under Different Hydraulic Gradients. Comput Geotech 105058
38. Xiong H, Wu H, Bao X, Fei J (2021) Investigating effect of particle shape on suffusion by CFD-DEM modeling. Constr Build Mater 289:123043
39. Kong Y, Guan M, Li X, et al How Flexible , Slit and Rigid Barriers Mitigate Two - phase Geophysical Mass Flows : A Numerical Appraisal. J Geophys Res Earth Surf. https://doi.org/10.1029/2021JF006587
40. Guo Y, Yang Y, Yu X (Bill) (2018) Influence of particle shape on the erodibility of non-cohesive soil: Insights from coupled CFD–DEM simulations. Particuology 39:12–24
41. Zhang F, Wang T, Liu F, et al (2020) Modeling of fluid-particle interaction by coupling the

discrete element method with a dynamic fluid mesh: Implications to suffusion in gap-graded soils. Comput Geotech 124:103617
42. Hu Z, Zhang Y, Yang Z (2019) Suffusion-induced deformation and microstructural change of granular soils: a coupled CFD–DEM study. Acta Geotech 14:795–814
43. Ke L, Takahashi A (2015) Drained monotonic responses of suffusional cohesionless soils. J Geotech Geoenviron Eng 141:1–8
44. Ouyang M, Takahashi A (2022) Mechanical consequence observation and microscopic visualization of internal erosion using developed plane strain erosion apparatus. Geotech Test J 45:0–3
45. Nguyen CD, Benahmed N, Andò E, et al (2019) Experimental investigation of microstructural changes in soils eroded by suffusion using X-ray tomography. Acta Geotech 14:749–765
46. Luo Y, Luo B, Xiao M (2020) Effect of deviator stress on the initiation of suffusion. Acta Geotech 15:1607–1617
47. Yang ZX, Lit XS, Yang J (2008) Quantifying and modelling fabric anisotropy of granular soils. Géotechnique 58:237–248
48. Guo N, Zhao J (2013) The signature of shear-induced anisotropy in granular media. Comput Geotech 47:1–15
49. Shire T, O'Sullivan C, Barreto D, Gaudray G (2013) Quantifying stress-induced anisotropy using inter-void constrictions. Géotechnique 63:85–91
50. Oda M, Nemat-Nasser S, Konishi J (1985) Stress-induced anisotropy in granular masses. Soils Found 25:85–97
51. Yang ZX, Yang J, Wang LZ (2013) Micro-scale modeling of anisotropy effects on undrained behavior of granular soils. Granul Matter 15:557–572
52. Gu X, Hu J, Huang M (2017) Anisotropy of elasticity and fabric of granular soils. Granul Matter 19:1–15
53. Luo Y, Luo B, Xiao M (2020) Effect of deviator stress on the initiation of suffusion. Acta Geotech 15:1607–1617
54. Qian JG, Zhou C, Yin ZY, Li WY (2021) Investigating the effect of particle angularity on suffusion of gap-graded soil using coupled CFD-DEM. Comput Geotech 139:104383
55. Xiong H, Yin ZY, Zhao J, Yang Y (2020) Investigating the effect of flow direction on suffusion and its impacts on gap-graded granular soils. Acta Geotech 16:399–419
56. Goniva C, Kloss C, Deen NG, et al (2012) Influence of rolling friction on single spout fluidized bed simulation. Particuology 10:582–591
57. Kenney TC, Lau D (1985) Internal stability of granular filters. Can Geotech J 22:215–225
58. Zeghal M, El Shamy U (2004) A continuum-discrete hydromechanical analysis of granular deposit liquefaction. Int J Numer Anal Methods Geomech 28:1361–1383
59. Shafipour R, Soroush A (2008) Fluid coupled-DEM modelling of undrained behavior of granular media. Comput Geotech 35:673–685
60. Volk A, Ghia U, Stoltz C (2017) Effect of grid type and refinement method on CFD-DEM solution trend with grid size. Powder Technol 311:137–146
61. Shan T, Zhao J (2014) A coupled CFD-DEM analysis of granular flow impacting on a water reservoir. Acta Mech 225:2449–2470
62. Li X, Zhao J (2018) A unified CFD-DEM approach for modeling of debris flow impacts on flexible barriers. Int J Numer Anal Methods Geomech 42:1643–1670

63. Yang ZX, Yang J, Wang LZ (2012) On the influence of inter-particle friction and dilatancy in granular materials: A numerical analysis. Granul Matter 14:433–447
64. Roux JN, Combe G (2010) How granular materials deform in quasistatic conditions. AIP Conf Proc 1227:260–270
65. Taha H, Nguyen NS, Marot D, et al (2019) Micro-scale investigation of the role of finer grains in the behavior of bidisperse granular materials. Granul Matter 21:1–17
66. Chang D (2012) Internal Erosion and Overtopping Erosion of Earth Dams and Landslide Dams
67. Aboul Hosn R, Sibille L, Benahmed N, Chareyre B (2018) A discrete numerical model involving partial fluid-solid coupling to describe suffusion effects in soils. Comput Geotech 95:30–39
68. Yimsiri S, Soga K (2010) DEM analysis of soil fabric effects on behaviour of sand. Géotechnique 60:483–495
69. Yang ZX, Wu Y (2017) Critical state for anisotropic granular materials: A discrete element perspective. Int J Geomech 17:1–15
70. Xiong H, Yin ZY, Zhao J, Yang Y (2020) Investigating the effect of flow direction on suffusion and its impacts on gap-graded granular soils. Acta Geotech 9:
71. Jiang MD, Yang ZX, Barreto D, Xie YH (2018) The influence of particle-size distribution on critical state behavior of spherical and non-spherical particle assemblies. Granul Matter 20:1–15
72. Thornton C, Antony SJ (2000) Quasi-static shear deformation of a soft particle system. Powder Technol 109:179–191
73. Farahnak Langroudi M, Soroush A, Tabatabaie Shourijeh P, Shafipour R (2013) Stress transmission in internally unstable gap-graded soils using discrete element modeling. Powder Technol 247:161–171
74. Ahmadi M, Shire T, Mehdizadeh A, Disfani M (2020) DEM modelling to assess internal stability of gap-graded assemblies of spherical particles under various relative densities, fine contents and gap ratios. Comput Geotech 126:103710
75. Radjai F, Wolf DE, Jean M, Moreau JJ (1998) Bimodal character of stress transmission in granular packings. Phys Rev Lett 80:61–64
76. Oda M (1972) Initial fabrics and their relations to mechanical properties of granular material. Soils Found 12:17–36
77. Zhang Y, Zhou X, Wen Y (2020) Constitutive theory for sand based on the concept of critical fabric surface. J Eng Mech 146:04020019
78. Shi DD, Cao D, Deng YB, Xue JF (2021) DEM investigations of the effects of intermediate principal stress ratio and particle breakage on the critical state behaviors of granular soils. Powder Technol 379:547–559
79. Sitharam TG, Vinod JS, Ravishankar B V. (2009) Post-liquefaction undrained monotonie behaviour of sands: Experiments and DEM simulations. Géotechnique 59:739–749
80. Zhao CF, Kruyt NP (2020) An evolution law for fabric anisotropy and its application in micromechanical modelling of granular materials. Int J Solids Struct 196–197:53–66